Table S1. Remote sensing products used in this study

Platform	Overpass [hr]	Sensor	Swath [km]	Pixel [km]	Product	AOD[1] 550nm	Short name	References
Terra	10:30AM	MODIS	2330	1	Dark Target C6.1	R	Terra-DT	Remer et al. (2005)
					Deep Blue C6.1	I/E	Terra-DB	Hsu et al. (2013, 2019); Sayer et al. (2019)
					MAIAC v2.0	E	Terra-MAIAC	Lyapustin et al. (2018)
					BAR v1.0	R	Terra-BAR	Lipponen et al. (2018)
ENVISAT	10:30AM	AATSR	500	1	ADV/ASV Ver2.30	R	AATSR-ADV	Sogacheva et al. (2017)
					ORAC v03.20	R	AATSR-ORAC	Thomas et al. (2009)
					AARDVARC v4.21	R	AATSR-SU	North et al. (1999); North (2002); Bevan et al. (2012)
Aqua	1:30PM	MODIS	2330	1	Dark Target C6.1	E	Aqua-DT	see Terra-DT
					Deep Blue C6.1	I/E	Aqua-DB	see Terra-DB
					MAIAC v2.0	E	Aqua-MAIAC	see Terra-MAIAC
					BAR v1.0	R	Aqua-BAR	see Terra-BAR
SeaSTAR	0:20PM	SeaWiFS	1502	13.5	Deep Blue & SOARv004	I/E R	SeaWiFS	Hsu et al. (2013); Sayer et al. (2012a, b)
noaa18	2:58PM	AVHRR	2900	8.8	Deep Blue & SOAR v001	E R	AVHRR	Hsu et al. (2017); Sayer et al. (2017)
AURA	1:30PM	OMI	2600	18	OMAERUV v1.7.1	E	OMAERUV	Ahn et al. (2014); Jethva et al. (2014)
PARASOL	1:30PM[2]	POLDER	1600	6.18	POLDER-GRASP-M v1.2	I	POLDER-GRASP	Dubovik et al. (2011); Chen et al. (2020)
PARASOL	1:30PM[2]	POLDER	1600	6.18	POLDER-RemoTAP	I	POLDER-RemoTAP	Lu et al. (2022); Hasekamp et al. (2024)

1) Interpolated or Extrapolated to 550 nm, depending on surface type; or Retrieved at 550 nm.
2) PARASOL started drifting away from Aqua at the end of 2009.

Table S2. AEROCOM models used in this study

Model full name	Model short name	Resolution latitude^o $\times$ longitude^o	Comments	References
PNNL CAM5.3	CAM5	1.875×2.5		Liu et al. (2012); Ghan et al. (2012)
CAM5.3-Oslo	CAM-Oslo	0.9735×1.25	a.k.a. NorESM	Kirkevåg et al. (2018)
ECHAM6.3-HAM2.3	ECHAM-HAM	1.875×1.875		Stier et al. (2005); Lohmann et al. (2007); Zhang et al. (2012)
ECHAM6-SALSA	ECHAM-SALSA	1.875×1.875		Stier et al. (2005); Bergman et al. (2012); Kokkola et al. (2018)
ECMWF-IFS-CY42R1-CAMS-RA	ECMWF-IFS	0.7031×0.7031		Rémy et al. (2019)
GEOS-Chem-v11-01	GEOS-Chem	1.978×2.5		Bey et al. (2001)
GEOS5-GOCART	GEOS5-replay	0.5×0.5		Colarco et al. (2010)
HadGEM3-GA7.1	HadGEM	1.25×1.875		
IMPACT	IMPACT	1.875×2.5		
LMDZORINCA_v6	INCA	1.259×2.5	external BC	Schulz et al. (2009); Wang et al. (2016)
OsloCTM3	OsloCTM	2.25×2.25		Myhre et al. (2009); Skeie et al. (2011); Lund et al. (2018)
MIROC5.9-SPRINTARS	SPRINTARS	0.563×0.563		Takemura et al. (2000); Takemura (2005, 2012)
TM5	TM5	2×3		van Noije et al. (2014, 2021)

Table S3. Parameters perturbed in the ECHAM-HAM and UKESM1-A PPEs. Empty entries indicate parameter not perturbed. A few parameters are missing for UKESM1-A as they did not seem to matter in the current study.

Process	Parameter name		Comments
	ECHAM-HAM	UKESM1-A	
Fossil Fuel emissions	EMI_FF		
Anthropogenic SO_2 emissions	EMI_ANTH_SO2	anth_so2	5 parameters for 5 regions
Volcanic SO_2 emissions		volc_so2	
Dimethyl Sulfide emissions	EMI_DMS	dms	
Sea-salt emissions	EMI_SS	sea_spray	
Primary marine organic emissions		prim_moc	
Biomass Burning emissions	EMI_BB		
BioFuel emissions	EMI_BF		
Dust emissions	EMI_DUST		
Biomass emitted particle size	EMI_CMR_BB	carb_bb_diam	
Biofuel emitted particle size	EMI_CMR_BF		
Fossil fuel emitted particle size	EMI_CMR_FF	carb_ff_diam	
Residential sources emitted particle size		carb_res_diam	
Primary SO_4 emitted particle size		pim_so4_diam	concerns only 50% of emissions
Width of Aitken mode		ait_width	
Dry deposition rate Aitken mode	DRYDEP_AIT	dry_dep_ait	
Dry deposition rate Accumulation mode	DRYDEP_ACC	dry_dep_acc	
Dry deposition rate SO_2		dry_dep_so2	
Dry deposition rate Coarse mode	DRYDEP_COA		
Wet deposition Below Cloud	WETDEP_BC		
Wet deposition In Cloud	WETDEP_IC		
Black Carbon Imaginary refractive index	BC_RAD_NI	bc_ri	
Dust Imaginary refractive index	DU_RAD_NI		
All SO_2 chemistry reaction rates	SO2REACTIONS		
Biogenic monoterpene SOA production rate		bvoc_soa	
Nucleation rate in Boundary Layer		bl_nuc	
Nucleation rate in Free Troposphere	NUC_FT		
Cloud PH for aqueous chemistry	PH_PERT	cloud_ph	
SO_4 hygroscopicity	KAPPA_SO4		
Organic carbon hygroscopicity		kappa_oc	
Sea-salt hygroscopicity	KAPPA_SS		
SO_4 layer thickness for aging	SO4COATING		
Ice fallspeed		m_ci	
Cloud top entrainment rate		a_ent_1_rp	

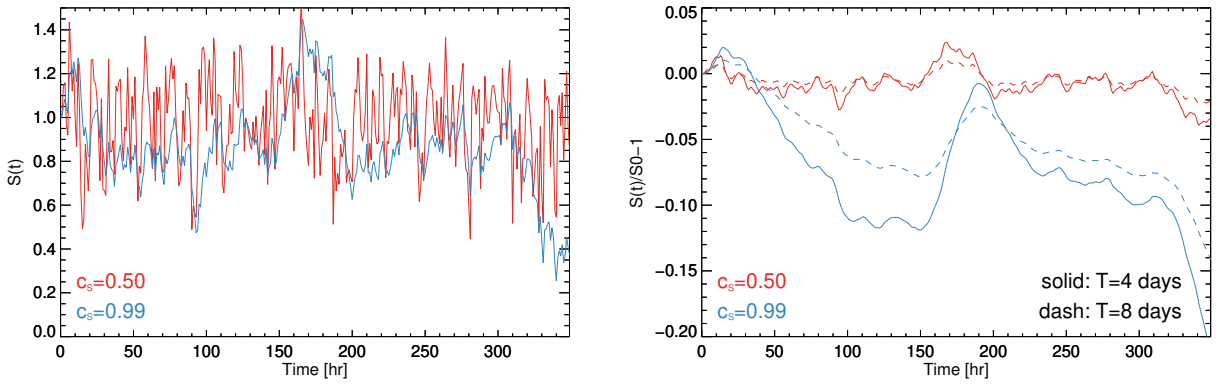

Figure S1. Examples of $S(t)$ and $m(t)$ generated from Eq. 6. The left panel shows two cases for $S(t)$, with either weakly correlated (red, $c_S = 0.5$) or strongly correlated (blue, $c_S = 0.99$) fluctuations. The right panel shows four cases of $m(t)$, for either a short (solid, $T = 4$ d) or a long (dashed, $T = 8$ d) life-time and either $S(t)$ scenario. The decorrelation time can be obtained from the $m(t)$ time-series and Eq. 4.

S1 Simple box model for a source with a rectangular pulse

We will consider a system that is in equilibrium, but experiences a rectangular pulse in its source term of duration Θ:

$$S(t) = \begin{cases} S_0 & \text{if } t < 0 \\ S_0 + \Delta S & \text{if } 0 \leq t \leq \Theta \\ S_0 & \text{if } t > \Theta \end{cases} \tag{S1}$$

The solution of Eq. 6 is now:

$$m(t) = \begin{cases} \frac{S_0}{k} & \text{if } t < 0 \\ \frac{S_0}{k} + \frac{\Delta S}{k}\left(1 - e^{-kt}\right) & \text{if } 0 \leq t \leq \Theta \\ \frac{S_0}{k} + \frac{\Delta S}{k}\left(e^{k\Theta} - 1\right)e^{-kt} & \text{if } t > \Theta \end{cases} \tag{S2}$$

Obviously, $< m(t) >= \frac{S_0}{k}$. By substituting $m(t) = m'(t) + \frac{S_0}{k}$, we can now rewrite Eq. 2 as:

$$\rho(\tau) = \frac{< m'(t)m'(t+\tau) >}{< m'(t)^2 >}, \tag{S3}$$

where the denominator is a special case of the numerator, which is:

$$< m'(t)m'(t+\tau) > = \lim_{\theta \to \infty} \frac{1}{2\theta} \int_{-\theta}^{\theta} m'(t)m'(t+\tau)dt. \tag{S4}$$

We can ignore the $\frac{1}{2\theta}$ as it occurs in both numerator and denominator, and concern ourselves with the integral only (which exists):

$$< m'(t)m'(t+\tau) > \propto \int_{-\infty}^{\infty} m'(t)m'(t+\tau)dt. \tag{S5}$$

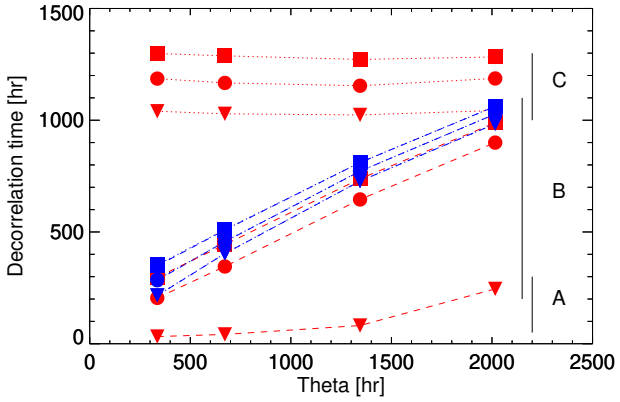

Figure S2. Decorrelation times τ_m^* versus pulse duration Θ (2, 4, 8 or 12 weeks) for several parameter combinations (c_S, T) in the simplebox model Eq. 6. Shown are averages over a sample of 100 times-series. Linestyles indicate c_S (dashed: low correlation, dotted: high correlation). The symbols indicate lifetime T (triangle: 1 day, circle: 6 days, square: 10 days). Colors indicate ratio of pulse amplitude to source fluctuations (red: 0.1, blue: 10). We distinguish three "regimes". A: uncorrelated fluctuations that are larger than the pulse; decorrelation time depends on lifetime with influence from pulse width. B: pulse amplitude is larger than fluctuations; decorrelation time is dominated by the pulse width. C: correlated fluctuations that are larger than the pulse; decorrelation time is dominated by the source fluctuations. Note that in all three regimes, there is usually a clear separation between different lifetimes, allowing them to be estimated if sufficient extra information on $S(t)$ is available.

For $\tau < \Theta$, this results in

$$< m'(t)m'(t+\tau) > \propto \frac{\Delta S^2}{k^3}\left\{k\Theta - k\tau - \tfrac{1}{2}\left(1-e^{-k\Theta}\right) - \left(1-e^{k\Theta}-\tfrac{1}{2}e^{-k\Theta}\right)e^{-k\tau} - \tfrac{1}{2}e^{-k\Theta}e^{k\tau}\right\} \quad \text{(S6)}$$

while for $\tau \geq \Theta$ we find:

$$< m'(t)m'(t+\tau) > \propto \frac{\Delta S^2}{k^3}\left(1-e^{-k\Theta}\right)\left(1-e^{k\Theta}\right)e^{-k\tau} \quad \text{(S7)}$$

From the latter relation we obtain ($\tau \geq \Theta$):

$$\rho(\tau) = e^{-k\tau} \quad \text{(S8)}$$

Note that if $\Theta > T = \frac{1}{k}$, the decorrelation time will be determined by Eq. S6 and not by Eq. S7.

S2 Impact from satellite sampling

The sampling of satellite data has a substantial effect on autocorrelations, just as it has on AOD (Schutgens et al., 2016). In this section we briefly discuss how sampling affects autocorrrelations in three different ways. To assess sampling impacts we will use the ECMWF-IFS model as a truth, which may then be sampled according to a satellite product.

First, there is a difference in the autocorrelation calculated from the full AOD data from ECMWF-IFS compared to the autocorrelation from ECMWF-IFS AOD sampled to a particular satellite product. The first is the autocorrelation we ideally

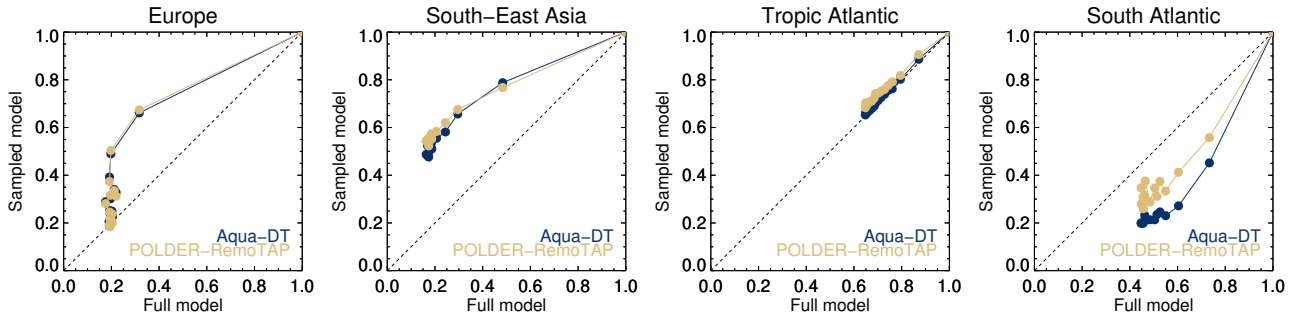

Figure S3. Impact of satellite sampling on autocorrelations at various lags (0-14 days). Each dot is the autocorrelation at a certain lag, the lines connect increasing lags (starting at (1,1) for a lag of zero). The autocorrelations are calculated from a synthetic truth (ECMWF-IFS model), using either the full model data (horizontal axis) or only the model data sampled to a satellite dataset (vertical axis, either RemoTAP or Aqua-DT). The dashed black line represents $y = x$. Only autocorrelations calculated over at least 30 datapoints are shown.

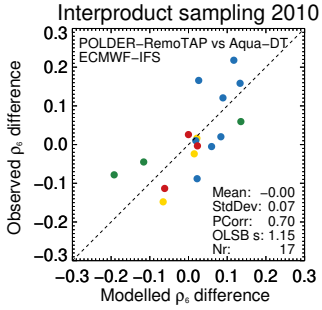

Figure S4. Impact of sampling on autocorrelations (at a lag of 6 days) for two different satellite products in 2010. The vertical axis shows the difference in ρ_6 for RemoTAP vs Aqua-DT (each product uses its own sampling). The horizontal axis shows the difference in ρ_6 for ECMWF-IFS, sampled to either RemoTAP or Aqua-DT. Each dot is ρ_6 for a particular region. Colours indicate regions (red: deserts, blue: ocean, green: biomass burning, yellow: North America, Europe, South-East Asia). The dashed black line represents $y = x$. Only autocorrelations calculated over at least 30 datapoints are shown.

want to know, the second is the autocorrelation we can actually observe. We note substantial differences, see Fig. S3. In general these differences result from the satellite not sampling the full diurnal cycle and not sampling the entire domain even at overpass. For many regions, results for RemoTAP and Aqua-DT are quite similar, even though the first product has substantially less observations. The relationships between ρ for the sampled and full dataset are nearly monotonically and often fairly linearly increasing, suggesting that the sampled dataset contains information about the full dataset.

Second, although it is not readily visible in the previous figure, there is a difference between autocorrelations from either RemoTAP or Aqua-DT, related to their sampling as is shown in Fig. S4. This analysis suggest that about 50% ($\text{PCorr}^2 = 0.49$)) of the difference in observed ρ is due to different orbits, swath widths, over pass times and pixel masking, all issues that determine the final sampling of a satellite product. We surmise the remaining 50% can be explained from observational errors in RemoTAP and Aqua-DT, which will be different, see Sect. 5 and 6, as well as errors in ECMWF-IFS to accurately model autocorrelations.

Third, there is a year-to-year variation in sampling that also leads to differences, see Fig. S5. The left two figures show that the year-to-year variation that might be observed in satellite products is not related to natural variation from year to year. The right two figures show that this year-to-year variation can to a significant extent be explained by satellite sampling, especially for RemoTAP which has, on the whole, less observations that Aqua-DT. This suggests that most of the variation seen from

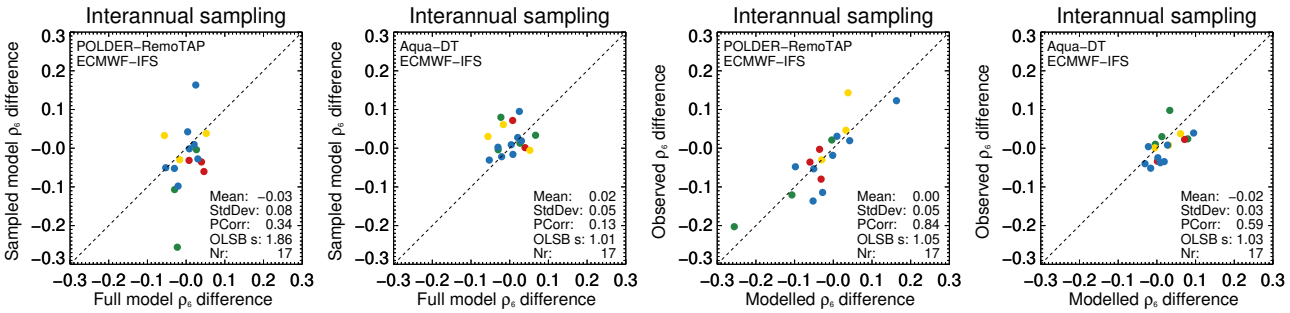

Figure S5. Impact of sampling from year to year on autocorrelations (at a lag of 6 days). The left two figures show a study based on only model data. The vertical axis shows autocorrelations calculated from sampled model data (sampled to a specific satellite product). The horizontal axis shows autocorrelations calculated from the full model data. The right two figures show a study based on both satellite observed and modelled autocorrelations (model was sampled to satellite product). In all cases what is shown is the autocorrelation in 2010 minus the autocorrelation in 2008. Each dot is ρ_6 for a particular region. Colours indicate regions (red: deserts, blue: ocean, green: biomass burning, yellow: North America, Europe, South-East Asia). The dashed black line represents $y = x$. Only autocorrelations calculated over at least 30 datapoints are shown.

year-to-year (Fig. 13 and 14) does not indicate natural variation. For Aqua-DT, which has many more observations, interannual differences are substantially smaller but can still to some extent be explained by sampling.

While satellite sampling can thus have a substantial impact on autocorrelations, proper collocation (see Sect. 2.5) of data ensures that the evaluation of satellite observed and modelled autocorrelations is possible.

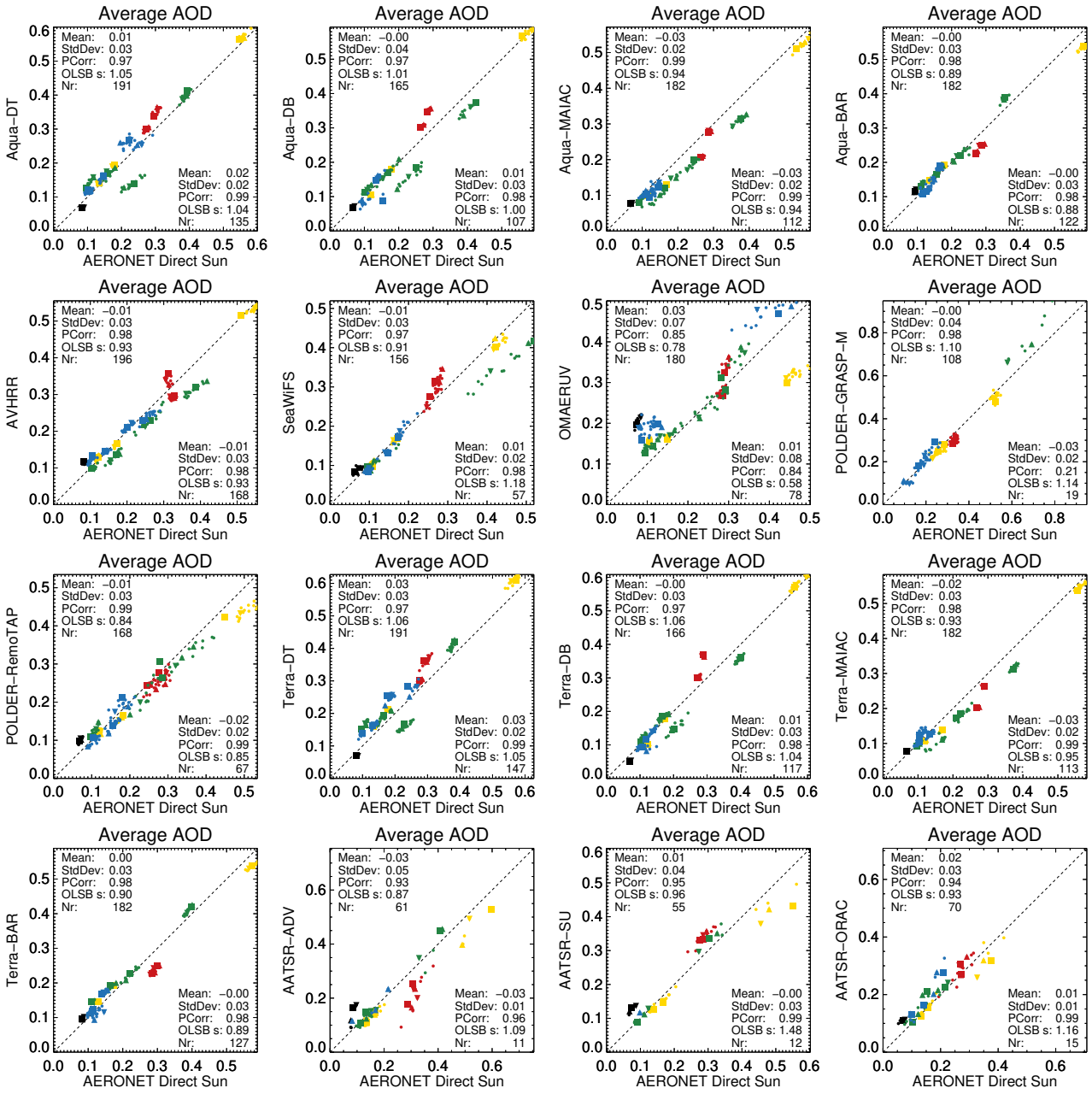

Figure S6. Evaluation of satellite observed regional averaged AOD with AERONET. Each symbol is the regional AOD for a specific region and lag. These autocorrelations are only shown if at least 30 data pairs were available to calculate autocorrelations. Colours indicate regions (red: deserts, blue: ocean, green: biomass burning, yellow: North America, Europe, South-East Asia, black: Australia). Symbols indicate lags (upward triangle: 3 days, square: 6 days, downward triangle: 9 days, dots: all other lags from 1 to 14 days). Statistics are shown for symbols based on at least 30 data pairs (upper left) or 300 (lower right, not shown for GRASP due to paucity of data). The mean, standard deviation, Pearson correlation and an unbiased slope estimate (OLSB) are shown for relevant symbols (Nr in total). The dashed black line represents $y = x$.

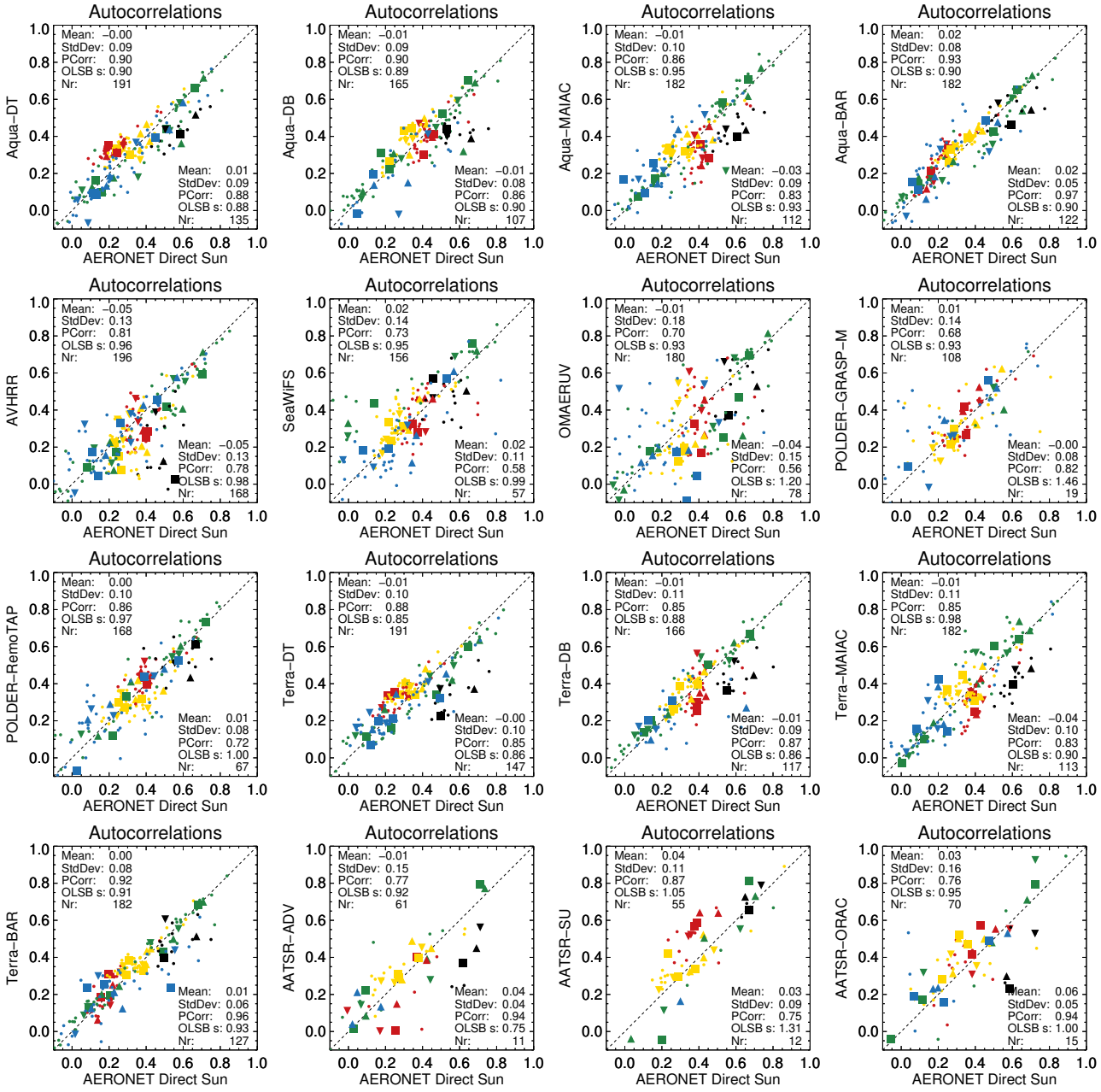

Figure S7. Evaluation of satellite observed autocorrelations with AERONET. Each symbol is the correlation for a specific region and lag. For more explanation, see the caption to Fig. S6

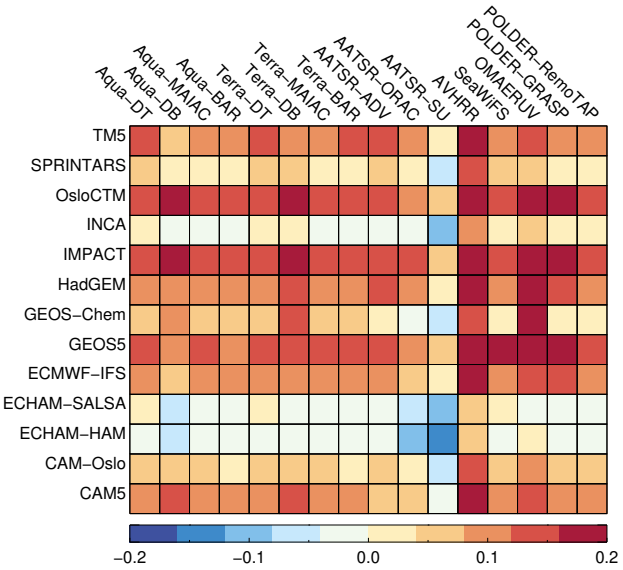

Figure S8. Model bias in autocorrelation at a lag of 6 days for all satellite products, as in Fig. 17. The models have been collocated to each product separately. Only region/lag cases with at least 3000 data pairs were used.

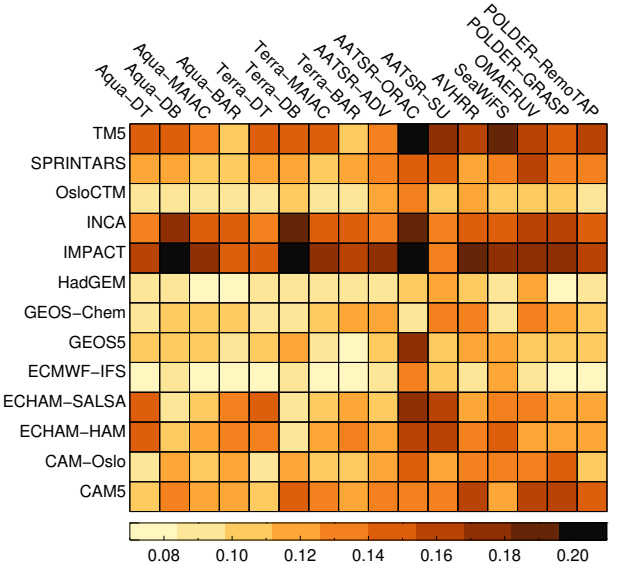

Figure S9. Standard deviation of the errors in model autocorrelation at a lag of 6 days for all satellite products, as in Fig. 17. The models have been collocated to each product separately. Only region/lag cases with at least 3000 data pairs were used.

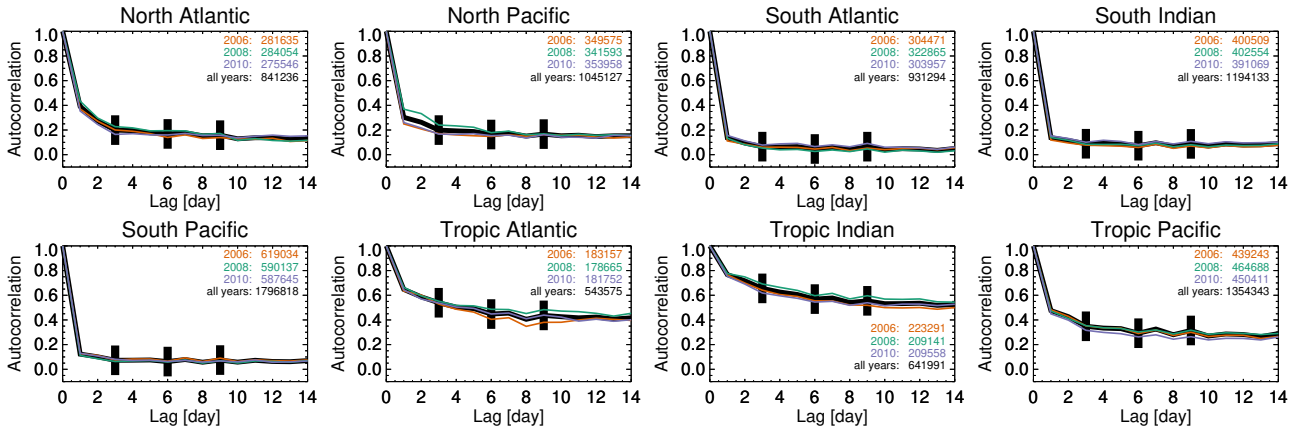

Figure S10. Temporal autocorrelations for a 3-year climatology from Aqua-DT (black) and the individual years (colors), for selected ocean regions. Also shown, for lags of 3, 6 and 9 days, are the σ uncertainty estimates from Sect. 6.

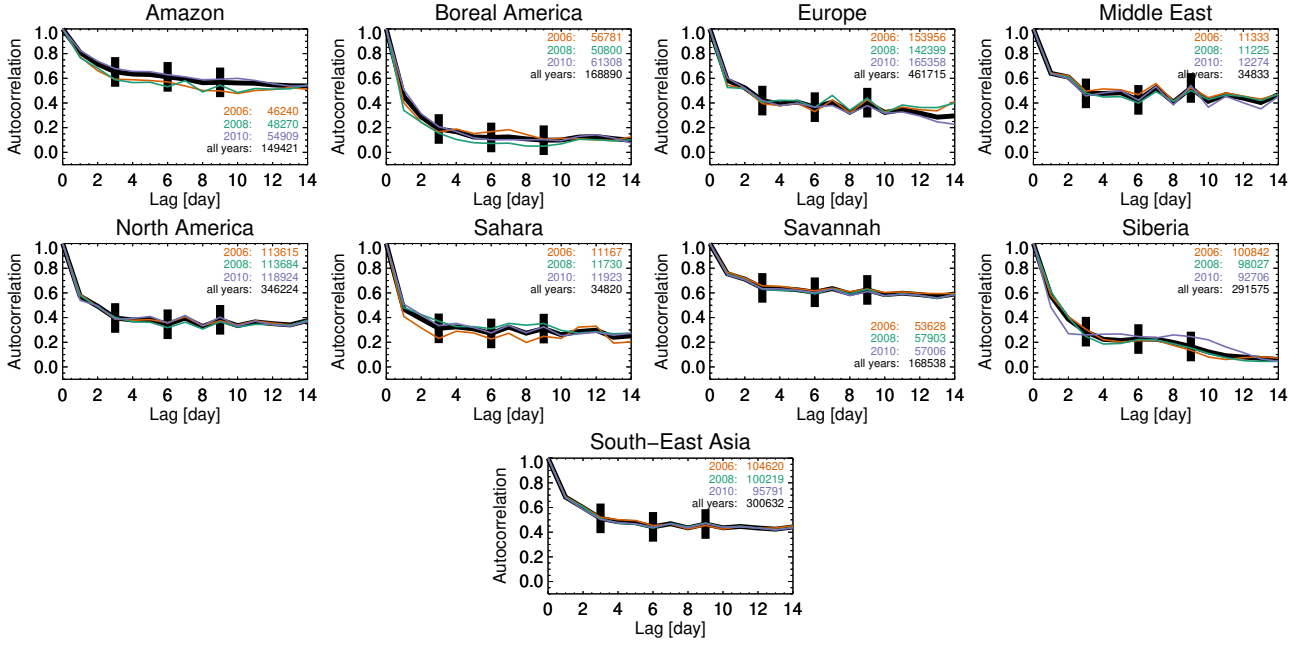

Figure S11. Temporal autocorrelations for a 3-year climatology from Aqua-DT (black) and the individual years (colors), for selected land regions. Also shown, for lags of 3, 6 and 9 days, are the σ uncertainty estimates from Sect. 6.

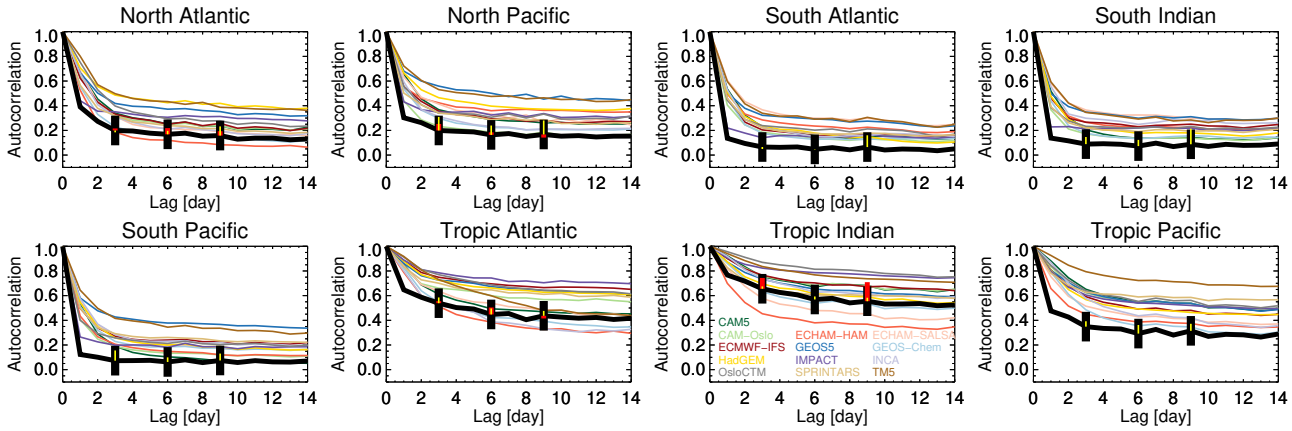

Figure S12. Temporal autocorrelations for AEROCOM models (colours) and Aqua-DT (black), for selected ocean regions. Also shown, for lags of 3, 6 and 9 days, are the 3σ uncertainty estimates from Sect. 6, as well as errors vs AERONET (in red, from Sect. 5) and Aqua-BAR (in yellow, from Sect. 6). Note that these uncertainties and errors were estimate for different sampling of Aqua-DT.

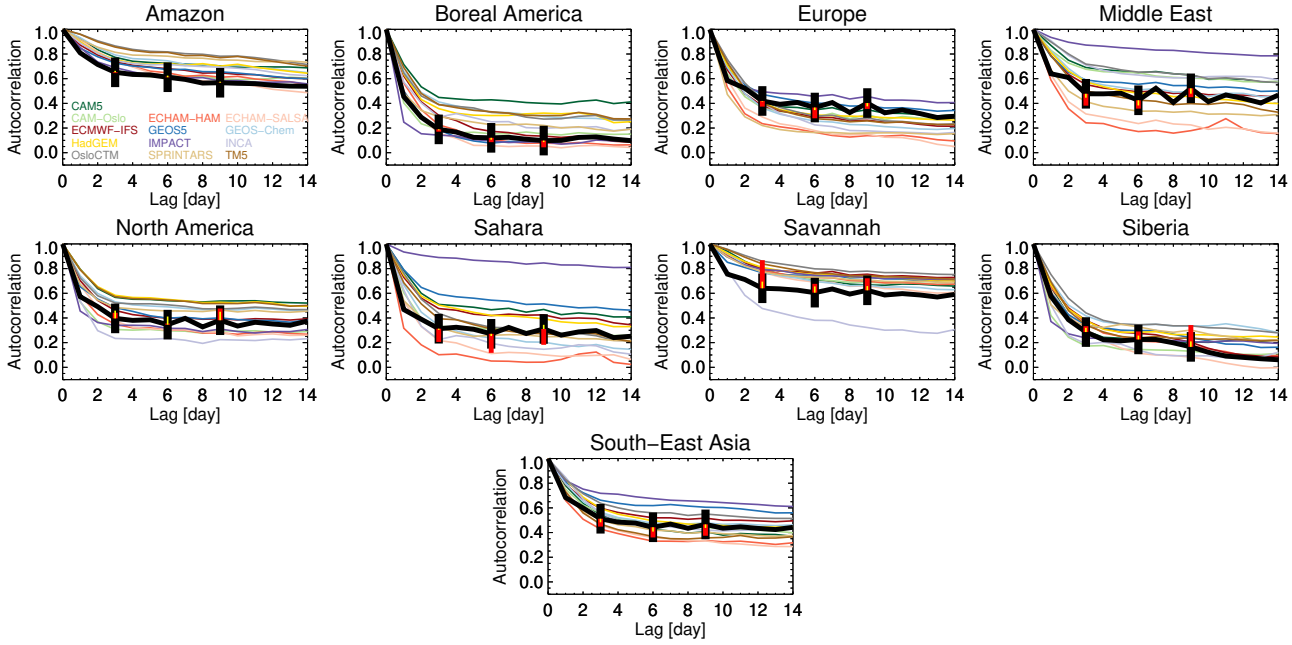

Figure S13. Temporal autocorrelations for AEROCOM models (colours) and Aqua-DT (black), for selected land regions. Also shown, for lags of 3, 6 and 9 days, are the 3σ uncertainty estimates from Sect. 6, as well as errors vs AERONET (in red, from Sect. 5) and Aqua-BAR (in yellow, from Sect. 6). Note that these uncertainties and errors were estimate for different sampling of Aqua-DT.

References

Ahn, C., Torres, O., and Jethva, H.: Assessment of OMI near-UV aerosol optical depth over land, Journal of Geophysical Research : Atmospheres, 119, 2457–2473, https://doi.org/10.1002/2013JD020188.Received, 2014.

Bergman, T., Kerminen, V., Korhonen, H., Lehtinen, K. J., Makkonen, R., Arola, A., and Mielonen, T.: Model Development Evaluation of the sectional aerosol microphysics module SALSA implementation in ECHAM5-HAM aerosol-climate model, Geoscientific Model Development, 5, 845–868, https://doi.org/10.5194/gmd-5-845-2012, 2012.

Bevan, S. L., North, P. R. J., Los, S. O., and Grey, W. M. F.: Remote Sensing of Environment A global dataset of atmospheric aerosol optical depth and surface re fl ectance from AATSR, Remote Sensing of Environment, 116, 199–210, https://doi.org/10.1016/j.rse.2011.05.024, 2012.

Bey, I., Jacob, D. J., Yantosca, R. M., Logan, J. A., Field, B. D., Fiore, A. M., Li, Q., Liu, H. Y., Mickley, L. J., and Schultz, M. G.: Global modeling of tropospheric chemistry with assimilated meteorology : Model description and evaluation, Journal of Geophysical Research: Atmospheres, 106, 73–95, 2001.

Chen, C., Dubovik, O., Fuertes, D., Litvinov, P., Lapyonok, T., Lopatin, A., Ducos, F., Derimian, Y., Herman, M., Tanré, D., Remer, L. A., Lyapustin, A., Sayer, A. M., Levy, R. C., Hsu, N. C., Descloitres, J., Li, L., Torres, B., Karol, Y., Herrera, M., Herreras, M., Aspetsberger, M., Wanzenboeck, M., Bindreiter, L., Marth, D., Hangler, A., and Federspiel, C.: Validation of GRASP algorithm product from POLDER / PARASOL data and assessment of multi-angular polarimetry potential for aerosol monitoring, Earth System Science Data, 12, 3573–3620, https://doi.org/10.5194/essd-12-3573-2020, 2020.

Colarco, P., Silva, A., Chin, M., and Diehl, T.: Online simulations of global aerosol distributions in the NASA GEOS - 4 model and comparisons to satellite and ground - based aerosol optical depth, Journal of Geophysical Research : Atmospheres, 115, https://doi.org/10.1029/2009JD012820, 2010.

Dubovik, O., Herman, M., Holdak, A., Lapyonok, T., Tanré, D., Deuzé, J. L., Ducos, F., Sinyuk, A., and Lopatin, A.: Statistically optimized inversion algorithm for enhanced retrieval of aerosol properties from spectral multi-angle polarimetric satellite observations, Atmospheric Measurement Techniques, 4, 975–1018, https://doi.org/10.5194/amt-4-975-2011, 2011.

Ghan, S. J., Liu, X., Easter, R. C., Zaveri, R., Rasch, P. J., Yoon, J.-H., and Eaton, B.: Toward a Minimal Representation of Aerosols in Climate Models: Comparative Decomposition of Aerosol Direct, Semidirect, and Indirect Radiative Forcing, Journal of Climate, 25, 6461–6476, https://doi.org/10.1175/JCLI-D-11-00650.1, 2012.

Hasekamp, O., Litvinov, P., Fu, G., Chen, C., and Dubovik, O.: Algorithm evaluation for polarimetric remote sensing of atmospheric aerosols, Atmospheric Measurement Techniques, 17, 1497–1525, https://doi.org/10.5194/amt-17-1497-2024, 2024.

Hsu, N., Lee, J., Sayer, A., Carletta, N., Chen, S.-H., Tucker, C., Holben, B., and Tsay, S.-C.: Retrieving near-global aerosol loading over land and ocean from AVHRR, Journal of Geophysical Research : Atmospheres, 122, 9968–9989, https://doi.org/10.1002/2017JD026932, 2017.

Hsu, N., Lee, J., Sayer, A., Kim, W., Bettenhausen, C., and Tsay, S.-C.: VIIRS Deep Blue Aerosol Products Over Land : Extending the EOS Long - Term Aerosol Data Records, Journal of Geophysical Research : Atmospheres, 124, 4026–4053, https://doi.org/10.1029/2018JD029688, 2019.

Hsu, N. C., Jeong, M., Bettenhausen, C., Sayer, A. M., Hansell, R., Seftor, C. S., Huang, J., and Tsay, S.: Enhanced Deep Blue aerosol retrieval algorithm : The second generation, Journal of Geophysical Research : Atmospheres, 118, 9296–9315, https://doi.org/10.1002/jgrd.50712, 2013.

Jethva, H., Torres, O., and Ahn, C.: Global assessment of OMI aerosol single-scattering albedo using ground-based AERONET inversion, Journal of Geophysical Research : Atmospheres, 119, 9020–9040, https://doi.org/10.1002/ 2014JD021672, 2014.

Kirkevåg, A., Grini, A., Olivié, D., Øyvind Seland, Alterskjær, K., Hummel, M., Karset, I. H. H., Lewinschal, A., Liu, X., Makkonen, R., Bethke, I., Griesfeller, J., and Schulz, M.: A production-tagged aerosol module for Earth system models , OsloAero5.3 – extensions and updates for CAM5.3-Oslo, Geoscientific Model Development, 11, 3945–3982, 2018.

Kokkola, H., Kühn, T., Laakso, A., Bergman, T., Lehtinen, K. E. J., Mielonen, T., Arola, A., Stadtler, S., Korhonen, H., Ferrachat, S., Lohmann, U., Neubauer, D., Tegen, I., Drian, C. S.-L., Schultz, M. G., Bey, I., Stier, P., Daskalakis, N., Heald, C. L., and Romakkaniemi, S.: SALSA2 . 0 : The sectional aerosol module of the aerosol – chemistry – climate model ECHAM6 . 3 . 0-HAM2 . 3-MOZ1 . 0, Geoscientific Model Development, pp. 3833–3863, 2018.

Lipponen, A., Mielonen, T., Pitkänen, M. R. A., Levy, R. C., and Sawyer, V. R.: Bayesian aerosol retrieval algorithm for MODIS AOD retrieval over land, Atmospheric Measurement Techniques, 11, 1529–1547, 2018.

Liu, X., Easter, R. C., Ghan, S. J., Zaveri, R., Rasch, P., Shi, X., Lamarque, J.-F., Gettelman, A., Morrison, H., Vitt, F., Conley, A., Park, S., Neale, R., Hannay, C., a. M. L. Ekman, Hess, P., Mahowald, N., Collins, W., Iacono, M. J., Bretherton, C. S., Flanner, M. G., and Mitchell, D.: Toward a minimal representation of aerosols in climate models: description and evaluation in the Community Atmosphere Model CAM5, Geoscientific Model Development, 5, 709–739, https://doi.org/10.5194/gmd-5-709-2012, 2012.

Lohmann, U., Stier, P., Hoose, C., Ferrachat, S., Kloster, S., Roeckner, E., and Zhang, J.: Cloud microphysics and aerosol indirect effects in the global climate model ECHAM5-HAM, Atmospheric Chemistry and Physics, 7, 3425–3446, https://doi.org/10.5194/acp-7-3425-2007, 2007.

Lu, S., Landgraf, J., Fu, G., van Diedenhoven, B., Wu, L., Rusli, S. P., and Hasekamp, O. P.: Simultaneous Retrieval of Trace Gases, Aerosols, and Cirrus Using RemoTAP—The Global Orbit Ensemble Study for the CO2M Mission, Frontiers in Remote Sensing, 3, https://doi.org/10.3389/frsen.2022.914378, 2022.

Lund, M. T., Myhre, G., Haslerud, A. S., Skeie, R. B., and Griesfeller, J.: Concentrations and radiative forcing of anthropogenic aerosols from 1750 to 2014 simulated with the Oslo CTM3 and CEDS emission inventory, Geoscientific Model Development, 11, 4909–4931, 2018.

Lyapustin, A., Wang, Y., Korkin, S., and Huang, D.: MODIS Collection 6 MAIAC algorithm, Atmospheric Measurement Techniques, 11, 5741–5765, 2018.

Myhre, G., Berglen, T. F., Johnsrud, M., Hoyle, C. R., Berntsen, T. K., a. Christopher, S., Fahey, D. W., a. Isaksen, I. S., a. Jones, T., a. Kahn, R., Loeb, N., Quinn, P., Remer, L., Schwarz, J. P., and Yttri, K. E.: Modelled radiative forcing of the direct aerosol effect with multi-observation evaluation, Atmospheric Chemistry and Physics, 9, 1365–1392, https://doi.org/10.5194/acp-9-1365-2009, 2009.

North, P. R. J.: Estimation of aerosol opacity and land surface bidirectional reflectance from ATSR-2 dual-angle imagery : Operational method and validation, Journal of Geophysical Research: Atmospheres, 107, 2002.

North, P. R. J., Briggs, S. A., Plummer, S. E., and Settle, J. J.: Retrieval of Land Surface Bidirectional Reflectance and Aerosol Opacity from ATSR-2 Multiangle Imagery, IEEE Trans. on Geoscience and Remote Sensing, 37, 526–537, 1999.

Remer, L., Kaufman, Y., Tanre, D., Mattoo, S., Chu, D., Martins, J., Li, R.-R., Ichoku, C., Levy, R., Kleidman, R., Eck, T., Vermote, E., and Holben, B.: The MODIS Aerosol Algorithm, Products, and Validation, J. Atmospheric Sciences, 62, 947 – 973, 2005.

Rémy, S., Kipling, Z., Flemming, J., Boucher, O., Nabat, P., Michou, M., Bozzo, A., Ades, M., Huijnen, V., Benedetti, A., Engelen, R., and henri Peuch, V.: Description and evaluation of the tropospheric aerosol scheme in the European Centre for Medium-Range Weather Forecasts (ECMWF) Integrated Forecasting System (IFS-AER , cycle 45R1), Geoscientific Model Development, 12, 4627–4659, 2019.

Sayer, A. M., Hsu, N. C., Bettenhausen, C., Ahmad, Z., Holben, B. N., Smirnov, A., Thomas, G. E., and Zhang, J.: SeaWiFS Ocean Aerosol Retrieval (SOAR): Algorithm , validation , and comparison with other data sets, Journal of Geophysical Research : Atmospheres, 117, 1–17, https://doi.org/10.1029/2011JD016599, 2012a.

Sayer, A. M., Hsu, N. C., Bettenhausen, C., Holben, B. N., Zhang, J., Technology, E. S., Forks, G., and Dakota, N.: Global and regional evaluation of over-land spectral aerosol optical depth retrievals from SeaWiFS, Atmospheric Measurement Techniques, 5, 1761–1778, https://doi.org/10.5194/amt-5-1761-2012, 2012b.

Sayer, A. M., Hsu, N. C., Lee, J., Carletta, N., Chen, S.-H., and Smirnov, A.: Evaluation of NASA Deep Blue / SOAR aerosol retrieval algorithms applied to AVHRR measurements, Journal of Geophysical Research : Atmospheres, 122, 9945–9967, https://doi.org/10.1002/2017JD026934, 2017.

Sayer, A. M., Hsu, N. C., Dutcher, S. T., and Lee, J.: Validation , Stability , and Consistency of MODIS Collection 6 . 1 and VIIRS Version 1 Deep Blue Aerosol Data Over Land, Journal of Geophysical Research : Atmospheres, 124, 4658–4688, https://doi.org/10.1029/2018JD029598, 2019.

Schulz, M., Cozic, A., and Szopa, S.: LMDzT-INCA dust forecast model developments and associated validation efforts, IOP Conference Series: Earth and Environmental Science, 7, 012 014, https://doi.org/10.1088/1755-1307/7/1/012014, 2009.

Schutgens, N., Partridge, D. G., and Stier, P.: The importance of temporal collocation for the evaluation of aerosol models with observations, Atmospheric Chemistry and Physics, 16, 1065–1079, https://doi.org/10.5194/acp-16-1065-2016, 2016.

Skeie, R. B., Berntsen, T. K., Myhre, G., Tanaka, K., and Kvalev, M. M.: Anthropogenic radiative forcing time series from pre-industrial times until 2010, Atmospheric Chemistry and Physics, 11, 11 827–11 857, https://doi.org/10.5194/acp-11-11827-2011, 2011.

Sogacheva, L., Kolmonen, P., Virtanen, T. H., Rodriguez, E., Saponaro, G., and de Leeuw, G.: Post-processing to remove residual clouds from aerosol optical depth retrieved using the Advanced Along Track Scanning Radiometer, Atmospheric Measurement Techniques, 10, 491–505, https://doi.org/10.5194/amt-10-491-2017, 2017.

Stier, P., Feichter, J., Kinne, S., Kloster, S., Vignati, E., Wilson, J., Ganzeveld, L., Tegen, I., and Werner, M.: The aerosol-climate model ECHAM5-HAM, Atmospheric Chemistry and Physics, 5, 1125–1156, 2005.

Takemura, T.: Simulation of climate response to aerosol direct and indirect effects with aerosol transport-radiation model, Journal of Geophysical Research, 110, D02 202, https://doi.org/10.1029/2004JD005029, 2005.

Takemura, T.: Distributions and climate effects of atmospheric aerosols from the preindustrial era to 2100 along Representative Concentration Pathways (RCPs) simulated using the global aerosol model SPRINTARS, Atmospheric Chemistry and Physics, 12, 11 555–11 572, https://doi.org/10.5194/acp-12-11555-2012, 2012.

Takemura, T., Okamoto, H., Maruyama, Y., Numaguti, A., Higurashi, A., and Nakajima, T.: Global three-dimensional simulation of aerosol optical thickness distribution of various origins, Journal of Geophysical Research, 105, 17 853, https://doi.org/10.1029/2000JD900265, 2000.

Thomas, G. E., Carboni, E., Sayer, A. M., Poulsen, C. A., Siddans, R., and Grainger, R. G.: Oxford-RAL Aerosol and Cloud (ORAC): aerosol retrievals from satellite radiometers, pp. 193–224, Springer, 2009.

van Noije, T., Bergman, T., Sager, P. L., O'Donnell, D., Makkonen, R., Gonçalves-Ageitos, M., Döscher, R., Fladrich, U., Hardenberg, J. V., Keskinen, J. P., Korhonen, H., Laakso, A., Myriokefalitakis, S., Ollinaho, P., Garciá-Pando, C. P., Reerink, T., Schrödner, R., Wyser, K., and Yang, S.: EC-Earth3-AerChem: A global climate model with interactive aerosols and atmospheric chemistry participating in CMIP6, Geoscientific Model Development, 14, 5637–5668, https://doi.org/10.5194/gmd-14-5637-2021, 2021.

van Noije, T. P. C., Sager, P. L., Segers, A. J., Velthoven, P. F. J. V., Krol, M. C., Hazeleger, W., and Williams, A. G.: Simulation of tropospheric chemistry and aerosols with the climate model EC-Earth, Geoscientific Model Development, pp. 2435–2475, https://doi.org/10.5194/gmd-7-2435-2014, 2014.

Wang, R., Balkanski, Y., Boucher, O., Ciais, P., Schuster, G. L., Chevallier, F., Samset, B. H., Liu, J., Piao, S., Valari, M., and Tao, S.: Estimation of global black carbon direct radiative forcing and its uncertainty constrained by observations, Journal of Geophysical Research, 121, 5948–5971, https://doi.org/10.1002/2015JD024326, 2016.

Zhang, K., O'Donnell, D., Kazil, J., Stier, P., Kinne, S., Lohmann, U., Ferrachat, S., Croft, B., Quaas, J., Wan, H., Rast, S., and Feichter, J.: The global aerosol-climate model ECHAM-HAM, version 2: Sensitivity to improvements in process representations, Atmospheric Chemistry and Physics, 12, 8911–8949, https://doi.org/10.5194/acp-12-8911-2012, 2012.